J Biol Inorg Chem (2014) 19:173–189
DOI 10.1007/s00775-013-1060-y

ORIGINAL PAPER

The effect of regioisomerism on the coordination chemistry and CEST properties of lanthanide(III) NB-DOTA-tetraamide chelates

Jacqueline R. Slack · Mark Woods

Received: 13 August 2013 / Accepted: 24 October 2013 / Published online: 28 November 2013

Abstract Chemical exchange saturation transfer (CEST) offers many advantages as a method of generating contrast in magnetic resonance images. However, many of the exogenous agents currently under investigation suffer from detection limits that are still somewhat short of what can be achieved with more traditional Gd^{3+} agents. To remedy this limitation we have undertaken an investigation of Ln^{3+} DOTA-tetraamide chelates (where DOTA is 1,4,7,10-tetraazacyclododecane-1,4,7,10-tetraacetic acid) that have unusually rigid ligand structures: the nitrobenzyl derivatives of DOTA-tetraamides with (2-phenylethyl)amide substituents. In this report we examine the effect of incorporating hydrophobic amide substituents on water exchange and CEST. The ligand systems chosen afforded a total of three CEST-active isomeric square antiprismatic chelates; each of these chelates was found to have different water exchange and CEST characteristics. The position of a nitrobenzyl substituent on the macrocyclic ring strongly influenced the way in which the chelate and Ln^{3+} coordination cage distorted. These differential distortions were found to affect the rate of water proton exchange in the chelates. But, by far the greatest effect arose from altering the position of the hydrophobic amide substituent, which, when forced upwards around the water binding site, caused a substantial reduction in the rate of water proton exchange. Such slow water proton exchange afforded a chelate that was 4.5 times more effective as a CEST agent than its isomeric counterparts in dry acetonitrile and at low temperatures and very low presaturation powers.

Keywords Conformational control · Lanthanide chelates · Macrocyclic ligands · Paramagnetic chemical exchange saturation transfer agents · Stereoisomerism

Introduction

Interest in the chemistry of macrocyclic lanthanide chelates has stemmed in large part from the use of gadolinium chelates as MRI contrast agents. Contrast media based on the Gd^{3+} ion are used to shorten the T_1 of the surrounding water, and in T_1-weighted magnetic resonance images (short echo and repetition times) this leads to an apparent brightening of regions to which the agent has been distributed. One requirement for a successful T_1-shortening Gd^{3+} chelate is that water molecules in the inner coordination sphere exchange very rapidly with those of the bulk solvent. This requirement has led to a historical focus on Gd^{3+} chelates of 1,4,7,10-tetraazacyclododecane-1,4,7,10-tetraacetic acid (DOTA) and its analogues at the expense of the related DOTA-tetraamide systems (Fig. 1). The Ln^{3+} chelates of DOTA-tetraamide ligands exhibit much slower

Responsible editor: Valerie C. Pierre.

Electronic supplementary material The online version of this article (doi:10.1007/s00775-013-1060-y) contains supplementary material, which is available to authorized users.

J. R. Slack · M. Woods (✉)
Department of Chemistry,
Portland State University,
1719 SW 10th Avenue,
Portland, OR 97201, USA
e-mail: mark.woods@pdx.edu; woodsmar@ohsu.edu

M. Woods
Advanced Imaging Research Center,
Oregon Health and Science University,
3181 SW Sam Jackson Park Road, Portland,
OR 97239, USA

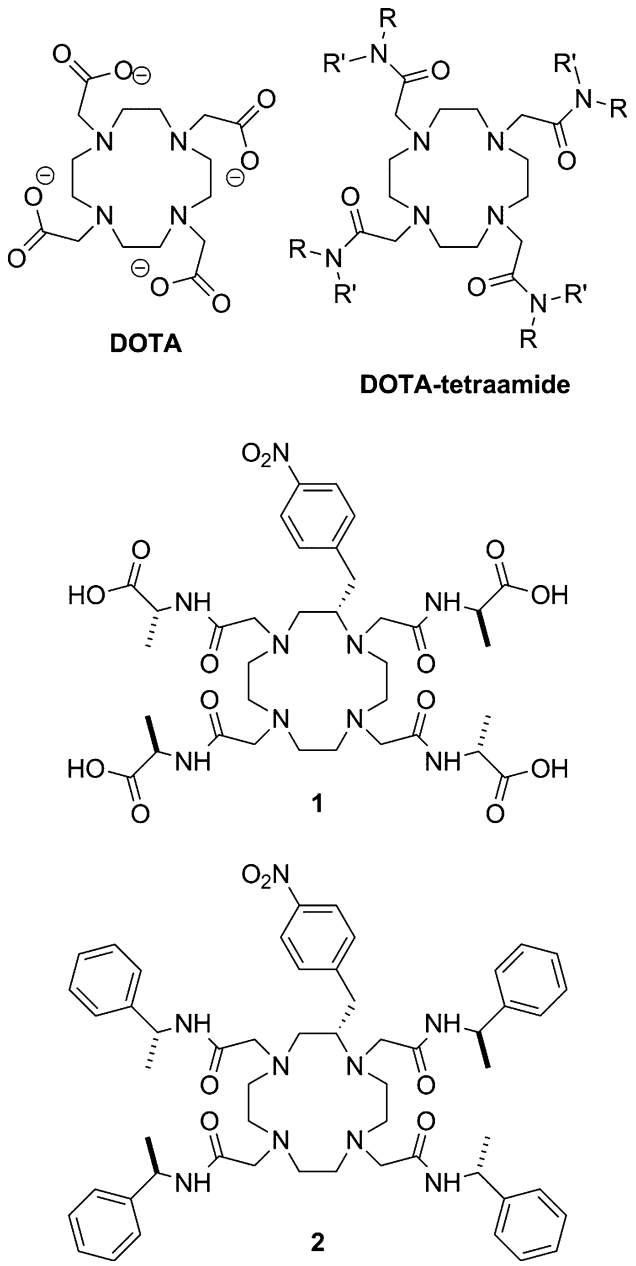

Fig. 1 The structural formulae of macrocyclic ligands derived from 1,4,7,10-tetraazacyclododecane and (*S*)-2-nitrobenzyl-1,4,7,10-tetraazacyclododecane. Ligands **1** and **2** were each produced as two stereoisomers: *S-RRRR* and *S-SSSS*

water exchange kinetics than those of DOTA, in large part because the neutral amide ligands are poorer electron donors than the anionic acetates of DOTA, rendering the Ln^{3+} ion more electron poor and in greater need of electron density from water molecules in the inner coordination sphere. Water molecules in the inner coordination sphere of DOTA-tetraamide chelates are held more tightly by the metal and exchange more slowly, rendering these chelates less effective as T_1-shortening agents. However, around the turn of the last century, Sherry and coworkers [1] realized that these slow exchange kinetics could be turned to an advantage. By substituting the Gd^{3+} ion, which has an isotropic *f* shell, for a paramagnetic Ln^{3+} ion with an anisotropic *f* shell, it is possible to induce very large shifts in the resonance frequency of coordinated water molecule protons [2]. These large shifts allow these paramagnetic chelates to be used as exogenous chemical exchange saturation transfer (CEST) contrast agents of the type proposed by Balaban and coworkers [3]. Balaban proposed diamagnetic CEST, but paramagnetic CEST (or paraCEST) offers certain advantages over diamagnetic and endogenous CEST. Firstly, the very large chemical shifts eliminate problems associated with direct off-resonance saturation of the solvent water that are common with diamagnetic agents. Secondly, they permit much faster exchange kinetics before the slow exchange limit is breached, potentially allowing for much more effective agents.

In the years since paraCEST contrast agents were first proposed, a variety of innovative agents have been reported showcasing some of the many potential advantages of this approach for generating image contrast. Of particular importance are the ability to develop ratiometric responsive probes; the ability to turn off contrast and interleave precontast and postcontrast acquisitions; the ability to perform "multicolored" imaging (imaging more than one agent simultaneously); and the ability to move beyond lanthanide chelates and use transition metal chelates. Rather than attempt to exhaustively cite the many demonstrations of these advantages, with the inevitable disappointment of those who are unintentionally overlooked, we direct the reader to some of the many reviews of this area for a more comprehensive picture of the field [4–14]. Despite all of these potential advantages, it is only recently that a concerted effort has been made to apply these exogenous paraCEST agents to in vivo imaging [15–21]. Some of this delay can be attributed to the relative inefficiency of many of the paraCEST agents proposed to date. Given the intense recent activity in this field, work investigating how structural modification of DOTA-tetraamide chelates might improve their function as paraCEST agents seems particularly timely. We have recently reported that the conformation of amide substituents in these chelates can profoundly alter the CEST properties of the agent [22]. Our initial idea had been that chiral substituents in the δ-position of the pendant arms of (*S*)-2-nitrobenzyl-1,4,7,10-tetraazacyclododecane [(*S*)-NB-cyclen] derived DOTA-tetraamides (NB-DOTA-tetraamides) would allow the coordination geometry of the chelate to be controlled in a manner analogous to that observed for α-substitution [23–27]. In reality this substitution did not afford control over the coordination geometry, but the results were more interesting that we had anticipated. Introducing a δ chiral carbon, as in Eu**1**$^{-}$, afforded some degree of control over

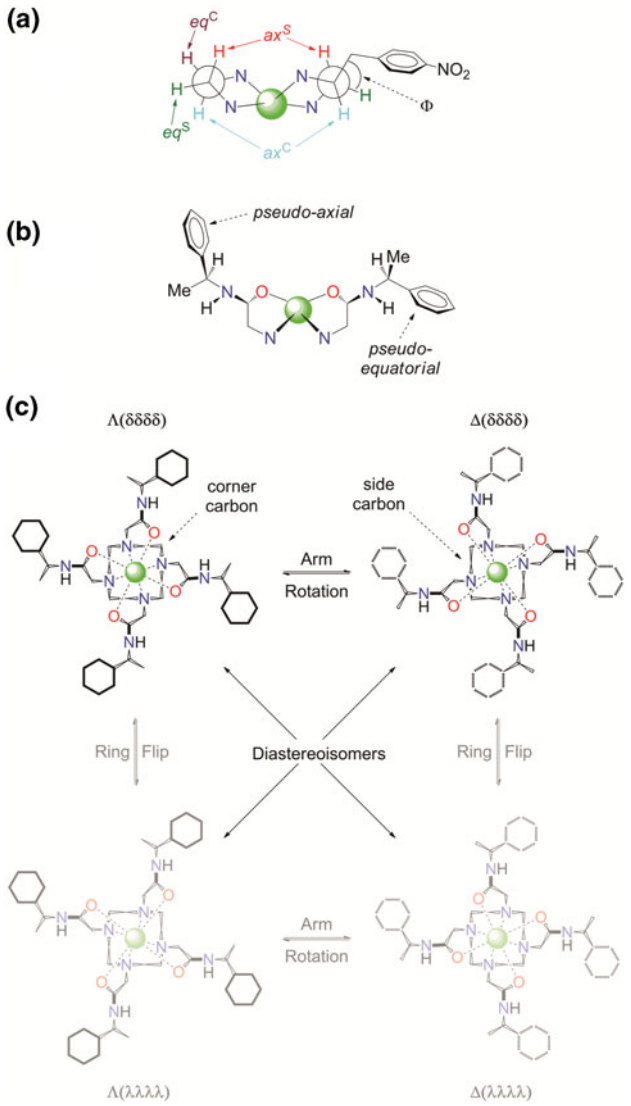

Fig. 2 Description of the nomenclature, and the structural and conformational parameters related to the chemistry of chiral DOTA-tetraamide chelates. **a** Designation of proton nomenclature for protons on the macrocyclic ring. **b** Description of the possible conformations of a chiral amide substituent (shown here with an *S* configuration) highlighting how the position of the bulky phenyl substituent changes depending on the orientation of the pendant arms, either Δ (*right*) or Λ (*left*). **c** Description of the four possible stereoisomeric coordination geometries of **2**. Λ(δδδδ) and Δ(λλλλ) are square antiprismatic (SAP) isomers, whereas Λ(λλλλ) and Δ(δδδδ) are twisted square antiprismatic (TSAP) isomers. The nitrobenzylic substituent on the macrocyclic ring has been omitted for clarity, although it may alternatively be positioned in the equatorial position on either the side or the corner carbon of one ethylene bridge. The two stereoisomeric structures rendered inaccessible by substitution of the macrocycle are washed out. In all structures the configuration at the δ-carbon is *S*

the position of the amide substituent; in this case a carboxylate. When this substituent was forced upwards into a pseudoaxial position (see Fig. 2b) towards the coordinated water molecule, the hydrophilic group was found to involve a greater number of water protons in the coordinated water molecule pool, increasing the CEST effect obtained by saturating the coordinated water molecule pool. In the current report we examine the effect of replacing the hydrophilic carboxylate with a hydrophobic phenyl substituent, $Eu\mathbf{2}^{3+}$, our starting hypothesis being that this should result in a substantial deceleration of the water exchange rate.

Materials and methods

General remarks

All solvents and reagents were purchased from commercial sources and used as received unless otherwise stated. The *S* and *R* isomers of 2-bromo-*N*-(1-phenylethyl)acetamide (**3**) were prepared according to previously described methods [28]. Purification by high-performance liquid chromatography (HPLC) was undertaken with a Waters δ-Prep 150 HPLC system using a Phenomenex Luna C-18(2) reversed-phase (50 mm × 250 mm) column. Elution was monitored by the absorption at 270 nm. All NMR spectra were recorded with a Bruker Advance IIa spectrometer operating at 400.13 MHz (^{1}H) and 100.61 MHz (^{13}C) using a 5-mm broadband probe with the temperature controlled using the installed BVT3200 variable-temperature controller with a BCU-05 chiller. Samples for two-dimensional correlation spectroscopy (COSY) were prepared in CD_3OD (99.8 atom %). Two-dimensional COSY spectra were acquired using 4,096 × 1,024 points using 16 transients per free induction decay at 263 K. Samples for CEST spectra were prepared in dry CD_3CN (99.8 atom %), and a known volume of H_2O was added. The concentration of each sample was determined by comparison of the intensity of the ^{19}F NMR signal with that of a 1.0 M solution of $Cu(OTf)_2$ (where OTf is trifluoromethanesulfonate, triflate) placed in a concentric insert in the NMR tube. CEST spectra were acquired at 275 K by measuring the water signal intensity as a function of the presaturation offset, in 1-ppm increments. The duration of the presaturation pulse was 10 s, with a $\boldsymbol{B}_1$ power of 148, 203, 279, 350, and 446 Hz.

(1*R*,4*R*,7*R*,10*R*)-δ,δ′,δ″,δ‴-Tetramethyl-[2-(*S*)-(*p*-nitrobenzyl)-1,4,7,10-tetraazacyclododecane]-1,4,7,10-tetra(2-phenylethyl)acetamide dihydrochloride salt

(*R*)-**3** (497 mg, 2.05 mmol), (*S*)-NB-cyclen (150 mg, 0.488 mmol), and potassium carbonate (337 mg, 2.44 mmol) were added to acetonitrile (50 mL). The resulting suspension was heated with stirring for 72 h at 333 K. Following addition of more (*R*)-**3** (83 mg, 0.34 mmol), the reaction mixture was heated for a further

48 h. After the mixture had cooled to room temperature, the solvents were removed under reduced pressure and the residue was divided between water (30 mL) and dichloromethane (200 mL). After separation, the aqueous phase was further extracted with dichloromethane (2 × 50 mL), the organic phases were combined and dried (Na_2SO_4), and the solvents removed under reduced pressure. The residue was taken up into a minimal amount of acetonitrile (6 mL) and purified by reversed-phase HPLC using a mobile phase of water (0.37 % HCl) for 5 min followed by a linear gradient over 20 min to 60 % acetonitrile and 20 % water (0.37 % HCl). After removal of the solvent by lyophilization, (1*R*,4*R*,7*R*,10*R*)-δ,δ′,δ″,δ‴-tetramethyl-[2-(*S*)-(*p*-nitrobenzyl)-1,4,7,10-tetraazacyclododecane]-1,4,7,10-tetra(2-phenylethyl)acetamide dihydrochloride salt (*S-RRRR*-**2**) was obtained as a colorless solid (1.4 g, 67 %).

R_T = 29.02 min. ^{1}H NMR (CH_3CN, 400 MHz) δ: 9.52 (2H, d, $^3J_{H-H}$ = 8 Hz, *p*-Ar), 8.04 (2H, d, $^3J_{H-H}$ = 8 Hz, *p*-Ar), 8.49 (2H, br, CON*H*), 8.38 (2H, br, CON*H*), 7.4–6.9 (20H, m, Ar), 4.91 (4H, m, C*H*CH_3), 4.78 [1H, dd (aa′ pattern), $^3J_{H-H}$ = 7 Hz, CH_2Ar], 4.76 [1H, dd (aa′ pattern), $^3J_{H-H}$ = 7 Hz, CH_2Ar], 2.5–3.9 (23H, m br, NCH_2 ring and NCH_2CO), 1.36 (12H, m, CH_3). ^{13}C NMR (CH_3CN, 100 MHz) δ: 20.9 (CH_3), 21.7 (CH_3), 22.0 (CH_3), 22.2 (CH_3), 32.6 (C$\underline{H}_2$Ar), 48.6, 48.8, 48.9, 49.0, 49.3, 49.5, 49.69, 50.2, 51.1, 51.6, 52.8, 53.3, 53.4, 54.7, 56.5, 56.6, 123.2, 123.5, 125.7, 125.9, 126.3–126.9 (several, overlapping), 128.0–128.4 (several, overlapping), 130.2, 143.3, 143.6, 143.9, 144.6, 144.9, 146.4, 146.7, 161.8 (C=O), 162.7 (C=O), 167.9 (C=O), 172.0 (C=O). Electrospray ionization (ESI) mass spectrometry (positive electron ionization) *m/z*: 952 (100 %, $[M + H]^+$).

(1*S*,4*S*,7*S*,10*S*)-δ,δ′,δ″,δ‴-Tetramethyl-[2-(*S*)-(*p*-nitrobenzyl)-1,4,7,10-tetraazacyclododecane]-1,4,7,10-tetra(2-phenylethyl)acetamide dihydrochloride salt

(1*S*,4*S*,7*S*,10*S*)-δ,δ′,δ″,δ‴-Tetramethyl-[2-(*S*)-(*p*-nitrobenzyl)-1,4,7,10-tetraazacyclododecane]-1,4,7,10-tetra(2-phenylethyl)acetamide dihydrochloride salt (*S-SSSS*-**2**) was prepared in an similar manner using (*S*)-**3**. After preparative reversed-phase HPLC, *S-SSSS*-**2** was obtained as a colorless solid (0.8 g, 52 %).

R_T = 29.84 min. ^{1}H NMR (CD_3CN, 400 MHz) δ: 7.97 (2H, d, $^3J_{H-H}$ = 8 Hz, *p*-Ar), 7.44 (20H, m, Ar), 7.31 (2H, d, $^3J_{H-H}$ = 8 Hz, *p*-Ar), 7.02 (4H, br, CON*H*), 4.91 (4H, m, C*H*CH_3), 4.76 (2H, s br, CH_2Ar), 2.1–2.7 (23H, m br, NCH_2 ring and NCH_2CO), 1.31 (12H, m, CH_3). ^{13}C NMR (CH_3CN, 100 MHz) δ: 21.2 (CH_3), 21.8 (CH_3), 22.1 (CH_3), 22.3 (CH_3), 36.4 (C$\underline{H}_2$Ar), 46.9, 47.8, 48.9, 49.0, 49.4, 49.6, 49.7, 49.8, 51.5, 51.8, 53.0, 53.3, 53.4, 53.7, 56.1, 57.0, 122.8, 125.5–126.9 (several, overlapping), 128.4–128.7 (several, overlapping), 131.4, 142.7, 143.0, 143.8, 144.9, 145.2, 146.7, 147.7, 162.0 (C=O), 162.5 (C=O), 168.5 (C=O), 171.4 (C=O). ESI mass spectrometry (positive electron ionization) *m/z*: 952 (100 %, $[M + H]^+$), 974 (46 %, $[M + Na]^+$).

General method for the preparation of Ln**2**$(OTf)_3$ chelates

The corresponding lanthanide triflate (73 μmol) was dissolved in (4 mL) and the mixture was added to a solution of either *S-RRRR*-**2** or *S-SSSS*-**2** (50 mg, 49 μmol) in 50:50 acetonitrile–water (4 mL). The resulting solution was heated with stirring for 24 h at 333 K. The solution was filtered through a 0.45-μm syringe filter and introduced directly into the HPLC system for purification. Purification was undertaken using a mobile phase of water (0.1 % trifluoroacetic acid) for 5 min, followed by a linear gradient to 10 % acetonitrile and 90 % water (0.1 % trifluoroacetic acid) over 15 min. Each chelate was collected from a single major peak in the chromatogram, and removal of the solvents by lyophilization afforded the chelate as the corresponding triflate salt as a colorless solid.

S-RRRR-Ce2(OTf)$_3$

High-resolution mass spectrometry (HRMS) [ESI time of flight (TOF) *m/z*: $[M]^{3+}$ calcd for $C_{55}H_{69}N_9CeO_6$ 363.8142; found 363.8135; $[M + OTf]^{2+}$ calcd for $C_{56}H_{69}F_3N_9CeO_9S$ 620.1973; found 622.1970. The appropriate Ce^{3+} isotope pattern was observed.

S-RRRR-Pr2(OTf)$_3$

HRMS (ESI-TOF) *m/z*: $[M]^{3+}$ calcd for $C_{55}H_{69}N_9PrO_6$ 364.1477; found 364.1472; $[M + OTf]^{2+}$ calcd for $C_{56}H_{69}F_3N_9PrO_9S$ 620.6976; found 620.6977. The appropriate Pr^{3+} isotope pattern was observed.

S-RRRR-Nd2(OTf)$_3$

HRMS (ESI-TOF) *m/z*: $[M]^{3+}$ calcd for $C_{55}H_{69}N_9NdO_6$ 364.4816; found 364.4806; $[M + OTf]^{2+}$ calcd for $C_{56}H_{69}F_3N_9NdO_9S$ 622.1996; found 622.1986. The appropriate Nd^{3+} isotope pattern was observed.

S-RRRR-Sm2(OTf)$_3$

HRMS (ESI-TOF) *m/z*: $[M]^{3+}$ calcd for $C_{55}H_{69}N_9SmO_6$ 367.6189; found 367.6175; $[M + OTf]^{2+}$ calcd for $C_{56}H_{69}F_3N_9SmO_9S$ 626.2044; found 626.2028. The appropriate Sm^{3+} isotope pattern was observed.

*S-RRRR-Eu**2**(OTf)$_3$*

HRMS (ESI-TOF) *m/z*: $[M]^{3+}$ calcd for $C_{55}H_{69}N_9EuO_6$ 368.1528; found 368.1538; $[M + OTf]^{2+}$ calcd for $C_{56}H_{69}F_3N_9EuO_9S$ 626.7052; found 622.7074. The appropriate Ce^{3+} isotope pattern was observed.

*S-RRRR-Tb**2**(OTf)$_3$*

HRMS (ESI-TOF) *m/z*: $[M]^{3+}$ calcd for $C_{55}H_{69}N_9TbO_6$ 370.1541; found 370.1533; $[M + OTf]^{2+}$ calcd for $C_{56}H_{69}F_3N_9TbO_9S$ 629.7072; found 629.7063. The appropriate Tb^{3+} isotope pattern was observed.

*S-RRRR-Dy**2**(OTf)$_3$*

HRMS (ESI-TOF) *m/z*: $[M]^{3+}$ calcd for $C_{55}H_{69}N_9DyO_6$ 371.8221; found 371.8213; $[M + OTf]^{2+}$ calcd for $C_{56}H_{69}F_3N_9DyO_9S$ 632.2092; found 632.2083. The appropriate Dy^{3+} isotope pattern was observed.

*S-RRRR-Er**2**(OTf)$_3$*

HRMS (ESI-TOF) *m/z*: $[M]^{3+}$ calcd for $C_{55}H_{69}N_9ErO_6$ 372.4891; found 372.4881; $[M + OTf]^{2+}$ calcd for $C_{56}H_{69}F_3N_9ErO_9S$ 634.2108; found 634.2098. The appropriate Er^{3+} isotope pattern was observed.

*S-RRRR-Yb**2**(OTf)$_3$*

HRMS (ESI-TOF) *m/z*: $[M]^{3+}$ calcd for $C_{55}H_{69}N_9YbO_6$ 375.1586; found 375.1589; $[M + OTf]^{2+}$ calcd for $C_{56}H_{69}F_3N_9YbO_9S$ 637.2140; found 637.2162. The appropriate Yb^{3+} isotope pattern was observed.

*S-SSSS-Ce**2**(OTf)$_3$*

HRMS (ESI-TOF) *m/z*: $[M]^{3+}$ calcd for $C_{55}H_{69}N_9CeO_6$ 363.8142; found 363.8133; $[M + OTf]^{2+}$ calcd for $C_{56}H_{69}F_3N_9CeO_9S$ 620.1973; found 620.1967. The appropriate Ce^{3+} isotope pattern was observed.

*S-SSSS-Pr**2**(OTf)$_3$*

HRMS (ESI-TOF) *m/z*: $[M]^{3+}$ calcd for $C_{55}H_{69}N_9PrO_6$ 364.1477; found 364.1473; $[M + OTf]^{2+}$ calcd for $C_{56}H_{69}F_3N_9PrO_9S$ 620.6976; found 620.6976. The appropriate Pr^{3+} isotope pattern was observed.

*S-SSSS-Eu**2**(OTf)$_3$*

HRMS (ESI-TOF) *m/z*: $[M]^{3+}$ calcd for $C_{55}H_{69}N_9EuO_6$ 368.1528; found 368.1537; $[M + OTf]^{2+}$ calcd for $C_{56}H_{69}F_3N_9EuO_9S$ 626.7052; found 626.7072. The appropriate Eu^{3+} isotope pattern was observed.

*S-SSSS-Tb**2**(OTf)$_3$*

HRMS (ESI-TOF) *m/z*: $[M]^{3+}$ calcd for $C_{55}H_{69}N_9TbO_6$ 370.1541; found 370.1532; $[M + OTf]^{2+}$ calcd for $C_{56}H_{69}F_3N_9TbO_9S$ 629.7072; found 629.7062. The appropriate Tb^{3+} isotope pattern was observed.

*S-SSSS-Dy**2**(OTf)$_3$*

HRMS (ESI-TOF) *m/z*: $[M]^{3+}$ calcd for $C_{55}H_{69}N_9DyO_6$ 371.8221; found 371.8208; $[M + OTf]^{2+}$ calcd for $C_{56}H_{69}F_3N_9DyO_9S$ 632.2092; found 632.2075. The appropriate Dy^{3+} isotope pattern was observed.

*S-SSSS-Ho**2**(OTf)$_3$*

HRMS (ESI-TOF) *m/z*: $[M]^{3+}$ calcd for $C_{55}H_{69}N_9HoO_6$ 372.1558; found 372.1547; $[M + OTf]^{2+}$ calcd for $C_{56}H_{69}F_3N_9HoO_9S$ 632.7097; found 632.7086. The appropriate Ho^{3+} isotope pattern was observed.

*S-SSSS-Er**2**(OTf)$_3$*

HRMS (ESI-TOF) *m/z*: $[M]^{3+}$ calcd for $C_{55}H_{69}N_9ErO_6$ 372.4891; found 372.4886; $[M + OTf]^{2+}$ calcd for $C_{56}H_{69}F_3N_9ErO_9S$ 634.2108; found 634.2001. The appropriate Er^{3+} isotope pattern was observed.

*S-SSSS-Yb**2**(OTf)$_3$*

HRMS (ESI-TOF) *m/z*: $[M]^{3+}$ calcd for $C_{55}H_{69}N_9YbO_6$ 375.1586; found 375.1599; $[M + OTf]^{2+}$ calcd for $C_{56}H_{69}F_3N_9YbO_9S$ 637.2140; found 622.2162. The appropriate Yb^{3+} isotope pattern was observed.

Results and discussion

Chelate preparation

The tetraamide derivatives of NB-cyclen pose a greater synthetic challenge than the corresponding acetate derivatives. In our experience, chelates derived from NB-cyclen do not crystallize, and this means that there are very few options for obtaining isomerically pure samples; our preferred method is to perform preparative reversed-phase HPLC. This has proven to be very effective for the preparation of hydrophilic anionic chelates in which the nitrobenzyl substituent causes substantial retention on a C_{18} stationary phase, requiring a fairly large proportion of

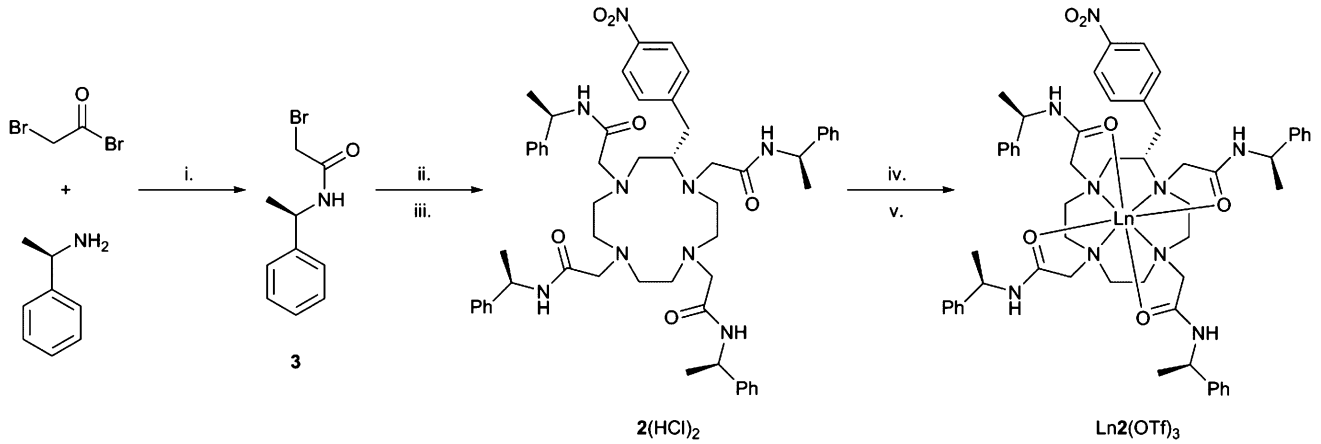

Scheme 1 The synthesis of $Ln\mathbf{2}^{3+}$ chelates shown for the *S-RRRR* isomer. The reagents and conditions were as follows: *i* 273 K/K_2CO_3/CH_2Cl_2; *ii* (*S*)-2-(*p*-nitrobenzyl)-1,4,7,10-tetraazacyclododecane/K_2CO_3/MeCN/333 K; *iii* purification by reversed-phase high-performance liquid chromatography; *iv* $Ln(OTf)_3$/MeCN/H_2O (pH 5.5)/333 K; *v* purification by reversed-phase high-performance liquid chromatography

acetonitrile in an aqueous solvent to induce elution [24]. A similar situation prevailed for the previously reported $Ln\mathbf{1}^-$ NB-DOTA-tetraamide chelates—the anionic substituents giving rise to monoanionic chelates. However, chelates of neutral NB-DOTA-tetraamide ligands afford trications, which seem to have higher affinity for the mobile phase and reduced affinity for the stationary phase (on a C_{18} column) and these chelates are much more readily eluted often even with pure aqueous solvent systems. This previously unpublished observation caused us to take a slightly different approach to the preparation of $Ln\mathbf{2}^{3+}$ chelates.

Two suitable alkylating agents—(*R*)-**3** and (*S*)-**3**—for the introduction of the pendant arms were prepared using previously published methods (Scheme 1) [28]. Samples of (*S*)-NB-cyclen were then alkylated with each bromoacetamide in acetonitrile using potassium carbonate as a base at 333 K for 3 days. Following removal of the solvents and aqueous workup, the oily residues were taken up into acetonitrile and purified by reversed-phase HPLC. The aim here was to remove all diastereoisomeric by-products at the ligand stage—although these should have been minimal because no transformation was undertaken at any chiral carbon—prior to producing the chelate, at which stage purification would be more challenging. Elution with water (0.37 % HCl) and acetonitrile afforded *S-RRRR*-**2** and *S-SSSS*-**2** as its corresponding dihydrochloride salt in the form of a colorless solid. Chelates of each ligand were prepared by dissolving *S-RRRR*-**2** and *S-SSSS*-**2** in a 50:50 mixture of acetonitrile and water and then adding an excess of the corresponding lanthanide triflate. The pH was adjusted to 5.5 with sodium hydroxide solution, and the solutions were heated at 333 K for 24 h. After the solvents had been removed by lyophilization, each chelate was analyzed by ^{1}H NMR spectroscopy. To our surprise, each sample was found to contain two chelates. At the time this work was undertaken this result was quite unexpected. The appearance of regioisomeric chelates was first noted by Ranganathan et al. [29] and is now well documented in rigid NB-DOTA derived chelates [26, 27], but was not previously noted during the preparation of $Ln\mathbf{1}^-$ chelates [22]. This may have been because at that time insufficient attention was paid to the identity of reaction by-products and the production of a second regioisomer during chelation was simply overlooked. However, it is important to note that the mechanism of chelate formation for acetate ligands, the step in which the two regioisomers differentiate, is quite different in tetraamide ligands [30]. Despite this difference and our previously proposed mechanisms [26] for the formation of each regioisomer, it is now clear that both acetate and amide chelation mechanisms can differentiate regioisomers, presumably dependent on the direction of approach of the metal ion. Each chelate was then subjected to a second round of HPLC purification to try and separate the two regioisomers. However, in all cases the chelates were eluted as a single major peak, which subsequent analysis by NMR spectroscopy and mass spectrometry showed contained two isomeric chelates. In consequence, only minor impurities and excess metal were removed during this second round of purification.

A second consideration must be borne in mind when purifying tricationic NB-DOTA-tetraamide chelates such as those of **2**. The nature of the counterion has been shown to have a significant effect on the properties of the chelate [31]. This was not a consideration during the preparation of the $Ln\mathbf{1}^-$ chelates since the chelate itself was the anion and the acidic eluent afforded the chelate as the conjugate acid. In previous studies on tricationic DOTA-tetraamides we tried to restrict the counterion to the convenient triflate

anion for reasons of consistency [32–34]. However, triflic acid is not a good additive to an HPLC eluent because excess acid is not readily removed under a vacuum. On the basis of our experience with anionic chelates, it was expected that retention on the HPLC column would effect anion exchange with the conjugate base of the eluent acid. For this reason the hydrochloric acid in the eluent was replaced with trifluoroacetic acid, the acid most like triflic acid that is suitable as an eluent additive. To our surprise, HRMS analysis of each Ln**2**$^{3+}$ chelate revealed the presence of triflate counterions after purification by reversed-phase HPLC, but no indication that either chloride or trifluoroacetate counterions were present. The view that each chelate was isolated as the triflate salt is further supported by ^{19}F NMR analysis, which revealed just a single peak, indicating that anion exchange with trifluoroacetate did not occur to any degree during purification of the chelates by reversed-phase HPLC. The interaction between Ln**2**$^{3+}$ chelates and the triflate counterions seems to be quite strong indeed, much stronger than that between the chelate and either chloride or trifluoroacetate. We may conclude, therefore, that after a second round of HPLC purification, all Ln**2**$^{3+}$ chelates were obtained as a mixture of two isomers in the form of the triflate salt, in which form all studies were performed.

Coordination chemistry of *S-RRRR*-Ln**2**$^{3+}$ chelates

The Ln^{3+} chelates of the 1,4,7,10-tetraazacyclododecane (cyclen)-derived analogue of **2** have been extensively studied by Dickins and Parker and their coworkers [34–38]. In common with other DOTA-tetraamides bearing bulky aromatic amide substituents, these chelates exhibit a marked preference for the square antiprismatic (SAP) coordination geometry [14, 32, 39]. DOTA-type ligands will sandwich an Ln^{3+} ion between the four coplanar nitrogen atoms of the macrocyclic ring and four coplanar oxygen atoms from the pendant arms (carboxylates, amides, phosphonates, phosphinates, etc.). This affords a very stable coordination mode which is usually, but not always, capped above the four pendant arm oxygen atoms by a coordinated water molecule. In this coordination mode (the only one observed for Ln^{3+} ions, although others are sometimes observed for transition metal ions) [40] both the macrocyclic ring and the pendant arms are defined by the helicity of their conformation: either δδδδ or λλλλ in the ring; and Δ or Λ in the arms (Fig. 2c). The relationship between these two conformations defines the coordination geometry of the chelate: when the two are opposed—Δ(λλλλ) and Λ(δδδδ)—the chelate adopts a SAP coordination geometry; when the two are the same—Λ(λλλλ) and Δ(δδδδ)—the chelate adopts a twisted square antiprismatic (TSAP) coordination geometry (Fig. 2c). Thus, four stereoisomeric structures are possible, and for Ln^{3+} chelates such as those of DOTA, all four conformations are accessible and in dynamic exchange. However, when substituents are introduced onto the pendant arm or the macrocyclic ring, the configuration at the resulting chiral carbon will help define the helicity of that component of the ligand. A popular substituent is a nitrophenyl, of which the nitro group is readily converted to the isothiocyanate, facilitating an easy conjugation to most primary amines. Nitrophenyl groups have been introduced in different positions of the ligand carbon skeleton with minimal effect on the performance of the chelates as contrast media, but with a significant effect on the coordination chemistry [41–43]. For instance, we have shown previously that introducing a nitrobenzyl substituent onto the cyclen ring, with an *S* configuration at carbon, freezes the macrocycle into the δδδδ conformation, minimizing torsional strain by placing the nitrobenzyl substituent in an equatorial position [43]. This conformational constraint is absolute in this case and the λλλλ conformation is effectively inaccessible even at relatively high temperatures. The Λ orientation of the pendant arms is congruent with the configuration at the δ-carbon (*R*), which means there is no force attempting to drive this chelate into a TSAP coordination geometry. However, two macrocyclic structures are still possible—this is because there are two distinct equatorial positions on the macrocyclic ring: one on the corner of the [3333] conformation and one on the side.

It is of little surprise that all the *S-RRRR*-Ln**2**$^{3+}$ chelates studied adopted a SAP coordination geometry. This is readily determined by examining the lanthanide-induced shifts (LIS) of the most shifted axial ring protons (ax^{S}) (Fig. 3) [44]. Because of the locking effect of the nitrobenzyl substituent a single stereochemistry is possible for this SAP coordination geometry: Λ(δδδδ). The two chelates observed in the ^{1}H NMR spectrum can arise only from regioisomerism of the nitrobenzyl substituent: either "side" or "corner." It is tempting to examine these NMR data to probe the change in regioisomeric distribution across the lanthanide series; however, this temptation must be resisted. The production of two regioisomers was not anticipated prior to preparation of the chelates and so reaction conditions from one Ln^{3+} to another were not carefully controlled. We have previously shown for NB-DOTMA chelates that factors such as pH and concentration have a measurable effect on the distribution of regioisomers [26]. One must also consider that these samples were subjected to preparative reversed-phase HPLC after the chelates had formed, and it is far from certain that for each sample the entirety of each peak was collected as it eluted—if the tail of a peak was cut off for one chelate but collected for another, this would introduce a sizable discrepancy in the observed isomeric distributions.

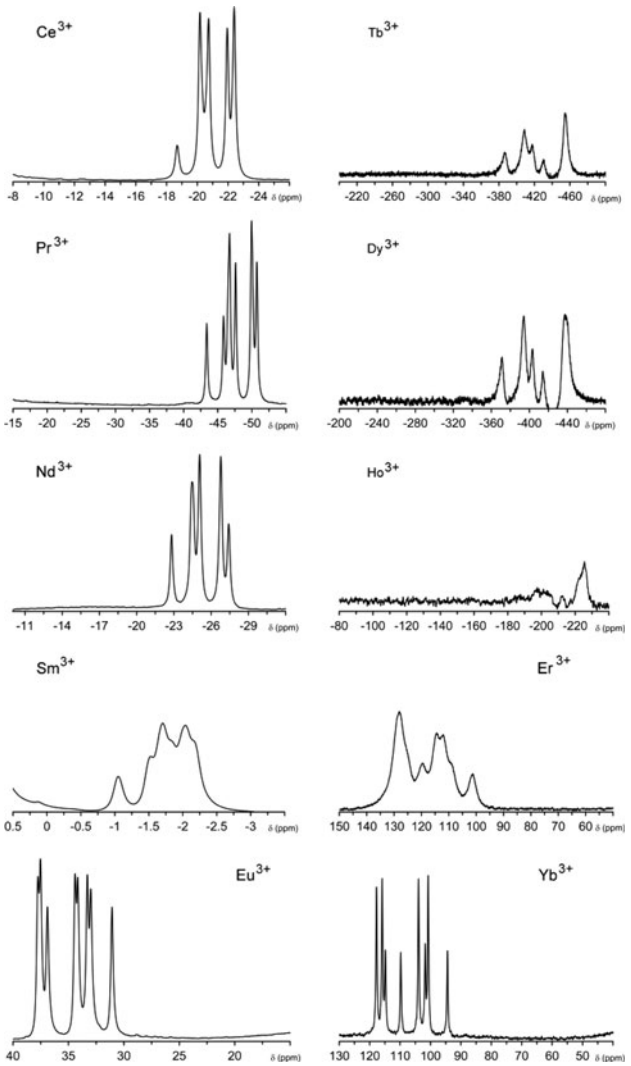

Fig. 3 The ^{1}H NMR spectra of *S-RRRR*-Ln**2**$^{3+}$ chelates recorded in CD_3OD at 400 MHz at 263 K, except for Dy^{3+} and Ho^{3+} (298 K). The spectra are expanded to show on the region in which only the ax^{S} proton resonances would be expected to appear. The spectra clearly show that all of the chelates adopt the SAP coordination geometry exclusively, but that in every case a mixture of side and corner isomers is observed

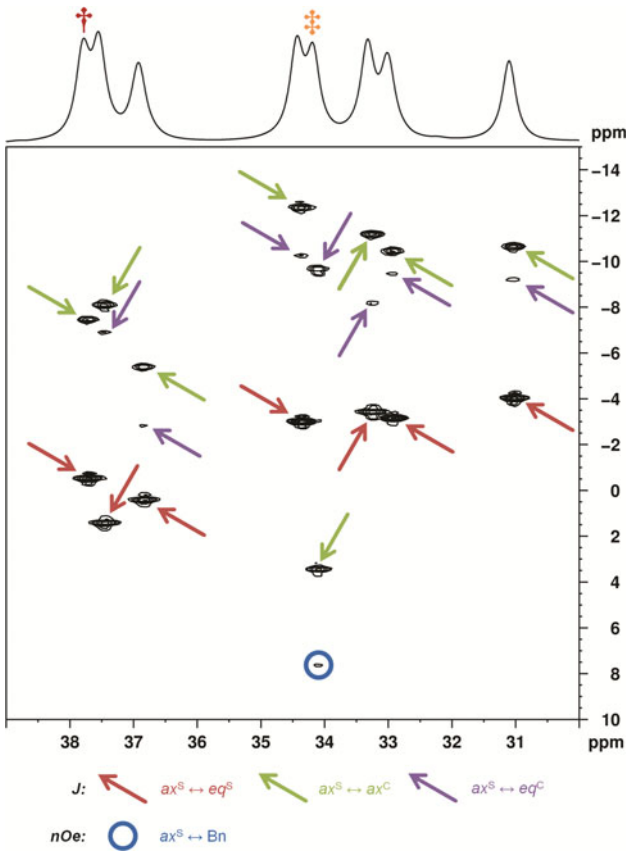

Fig. 4 The ^{1}H–^{1}H correlation spectroscopy (COSY) spectrum of *S-RRRR*-Eu**2**$^{3+}$ expanded to show only the couplings to the four ax^{S} protons of each chelate. The spectrum was acquired in CD_3OD at 400 MHz and 263 K. The resonances of the proton on the nitrobenzyl-substituted carbons are identified by a *double dagger* (side isomer) and a *dagger* (corner isomer). *nOe* nuclear Overhauser effect

The two regioisomers can be identified through ^{1}H–^{1}H COSY experiments. The COSY spectrum of *S-RRRR*-Eu**2**$^{3+}$ is shown in Fig. 4. For six of the eight ax^{S} resonances, three *J* couplings are evident. In order of decreasing magnitude they are a geminal ax^{S}–eq^{S} coupling, a vicinal ax^{S}–ax^{C} coupling, and a vicinal ax^{S}–eq^{C} coupling, as described in Fig. 2a. It is notable that the most shifted resonance is coupled to only two other protons. From the magnitude of these couplings and the shifts of the protons to which it is coupled, it is possible to conclude that the equatorial proton on the carbon at the corner of the ring (eq^{C}) is absent, i.e., the nitrobenzyl substituent is located on this ethylene bridge, but on the carbon at the corner of the ring. In contrast, the resonance just downfield of 34 ppm exhibits three couplings, but none are of sufficient magnitude to be a geminal coupling. Furthermore, one of these couplings is to a benzylic proton at about 8 ppm—this is not a *J* coupling but, as observed in the COSY spectra of NB-DOTMA [27], is a nuclear Overhauser effect cross-peak that arises from the proximity of this proton to the benzylic protons of the nitrobenzyl substituent. This indicates that this isomer has the nitrobenzyl group located on this carbon, adjacent to this proton; i.e., the substituent is located on the side of the macrocyclic ring. One further observation is worthy of note: the magnitude of the vicinal ax^{S}–eq^{C} coupling is significantly larger on this ethylene bridge than all the others in the spectrum. Curiously in the case of NB-DOTMA [27], and even NB-DOTA [43], the magnitude of this coupling was found to be smaller than those of the other ethylene bridges, and on occasion so much smaller that it was not observed in the spectrum. In light of the Karplus relationship [45], one must conclude that in each case the ethylene bridge is being distorted by

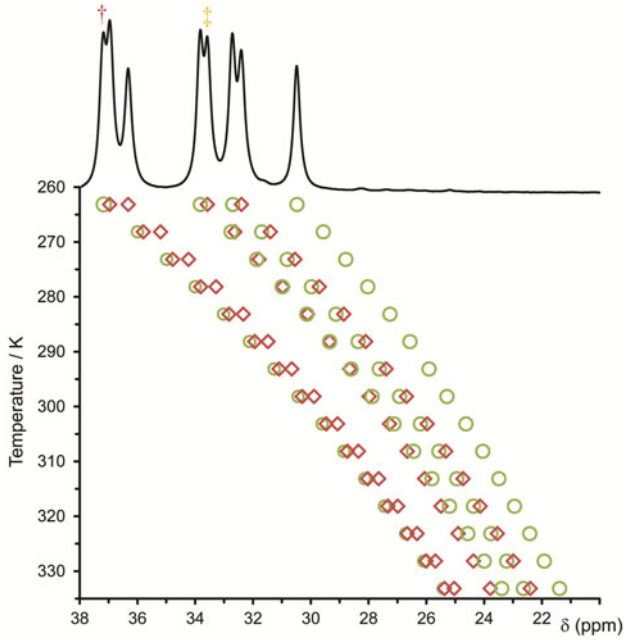

Fig. 5 The effect on temperature of the ax^S protons shifts of *S-RRRR*-Eu**2**$^{3+}$ at 400 MHz in CD_3OD. The resonances arising from the corner isomer are denoted by *circles*, and those arising from the side isomer are denoted by *diamonds*. The protons adjacent to the nitrobenzyl substituent are denoted by a *dagger* (corner) and a *double dagger* (side)

the nitrobenzyl substituent. In an ideal [3333] ring conformation each ethylene bridge adopts a gauche conformation, but if the ethylene bridge distorts in such a way as to make the angle (Φ) between the ax^S and eq^C protons greater the *J* coupling between these two protons will decrease, as observed previously for NB-DOTMA derivatives [27]. Because this vicinal *J* coupling increases in the side isomer of *S-RRRR*-Eu**2**$^{3+}$, the ethylene bridge on which the nitrobenzyl substituent is located must be distorting in the opposite direction, making the ax^S–eq^C angle (Φ) smaller (Fig. 2a).

One further point should be addressed: the ^{1}H NMR data shown herein are generally obtained in CD_3OD and at low temperatures. The reason for this is that it was frequently found that the spectral lines of these chelates acquired in CD_3CN and/or at room temperature were quite broad. However, switching the solvent to CD_3OD had two effects: the lines tended to be sharper but the LIS tended to be smaller. This observation is consistent with the solvent interacting directly with the Ln^{3+} ion in the apical position usually occupied with water. Dickins et al. [34] found that in this position, CD_3CN would induce larger LIS than CD_3OD, which induces LIS of a similar order of magnitude as water. This could then be the origin of the line broadening observed in these chelates. In the presence of only traces of water, the chelates undergo ligand exchange in the apical position that is of intermediate rate on the NMR timescale, resulting in broad lines. In fact, in experiments described later samples of some chelates were prepared in CD_3CN and small amounts of water were added. In some cases when insufficient water had been added, and the NMR spectra were acquired at 263 K, resonances from both the CH_3CN-ligated and H_2O-ligated chelates could be clearly resolved (Fig. S1). Because both water and CD_3OD induced very similar LIS, the ligand exchange reaction can very easily enter the fast exchange regime, affording sharper lines. However, to achieve better spectral resolution through increased LIS, it was often desirable to acquire NMR data in CD_3OD at low temperatures. This line of reasoning was supported by the observation that some of the later lanthanides, which induce much larger LIS, would often afford broader lines at lower temperatures in CD_3OD, presumably because the ligand exchange reaction had been slowed to an intermediate exchange regime. Nonetheless, there is an alternative explanation for the observed line broadening; that is, that the two regioisomers themselves are in chemical exchange. If that were the case, then as the temperature of the sample is increased, the resonances should consistently move towards one another. In NB-DOTMA chelates we have observed that it is possible to interconvert the two regioisomers only by demetallation of the chelate [26], a process that does not occur on the NMR timescale, but to rule out this possibility, a variable-temperature ^{1}H NMR experiment was undertaken on *S-RRRR*-Eu**2**$^{3+}$ (Fig. 5).

The shifts of all the ax^S resonances decrease with increasing temperature, which is consistent with the inverse correlation of both the dipolar and the contact contributions to the LIS with temperature. However, it is notable that none of the resonances move closer together in a consistent manner, and significantly the two nitrobenzyl-substituted peaks remain as far apart at high temperature as they do at low temperature. We may therefore conclude that, like their acetate analogues, the regioisomers of NB-DOTA-tetraamide derivatives are not in chemical exchange and the line broadening observed in CD_3CN solution is the result of ligand exchange reactions on the intermediate timescale.

Coordination chemistry of *S-SSSS*-Ln**2**$^{3+}$ chelates

The coordination chemistry of *S-SSSS*-Ln**2**$^{3+}$ chelates is richer and more complex than that of the *S-RRRR* isomers. Here again the conformation of the macrocyclic ring is locked into a δδδδ conformation by the nitrobenzyl substituent. But in this case the configuration at the δ chiral carbon of each pendant arm (*S*) is opposed to the helicity required (Λ) for the chelate to adopt a SAP coordination geometry. This means that each chelate has two choices:

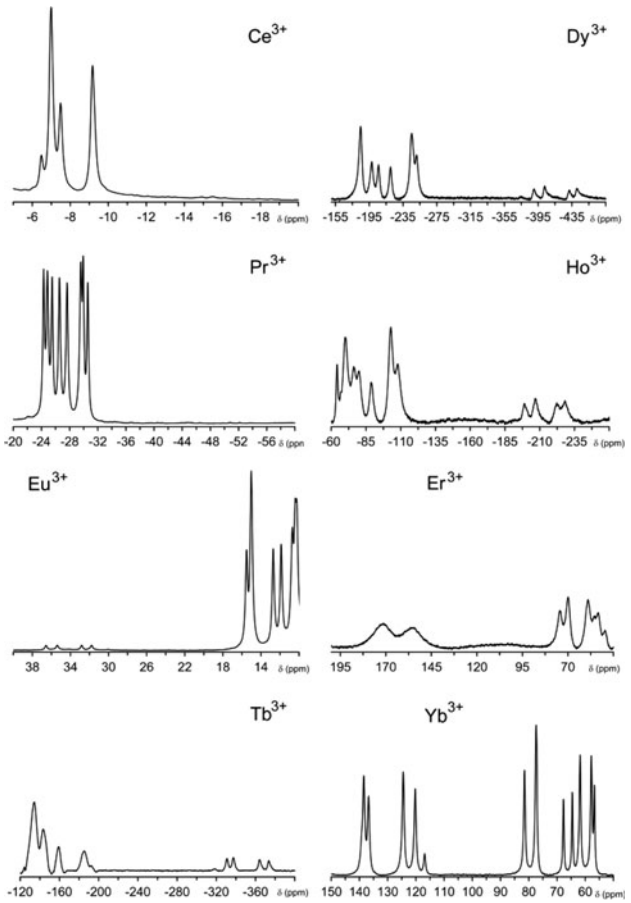

Fig. 6 The ^{1}H NMR spectra of *S-SSSS*-Ln**2**$^{3+}$ chelates expanded to focus on the region in which the most shifted ax^{S} protons are expected to appear. The spectra were recorded in CD_3OD at 400 MHz and 263 K, except for Tb^{3+}, Dy^{3+}, Ho^{3+}, and Er^{3+} (298 K)

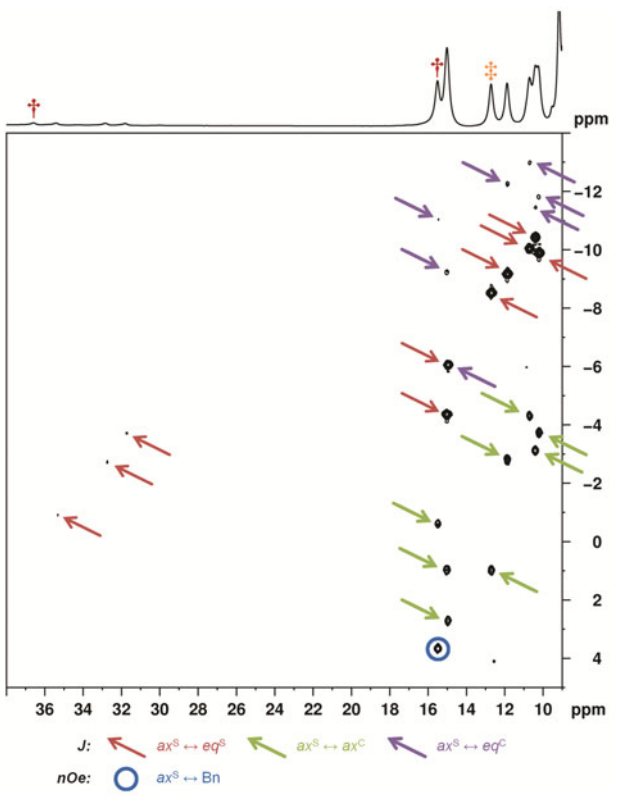

Fig. 7 The ^{1}H–^{1}H COSY spectrum of *S-SSSS*-Eu**2**$^{3+}$ expanded to show only the couplings to the ax^{S} protons of each chelate. The spectrum was acquired in CD_3OD at 400 MHz and 263 K. The protons adjacent to the nitrobenzyl substituent are denoted by a *red dagger* (side) and *yellow double dagger* (corner)

either position the pendant arms in the Δ orientation preferred by an *S* configuration and adopt a TSAP coordination geometry, or force the arms into a Λ orientation, pushing the bulky phenyl substituents into a less favorable pseudoaxial position above the chelate and adopt a SAP coordination geometry (Fig. 2). For the early lanthanides the choice is clear. The larger ionic radius of the early Ln^{3+} ions is readily accommodated by the more open TSAP geometry [46, 47] and the Ce^{3+} and Pr^{3+} chelates of *S-SSSS*-**2** adopt this coordination geometry exclusively (Fig. 6). However, as the ionic radius of the Ln^{3+} ion decreases, the innate preference for the SAP coordination geometry begins to win out. Thus, we see that in the ^{1}H NMR spectrum of *S-SSSS*-Eu**2**$^{3+}$ small amounts of the SAP isomer are present, and as the Ln^{3+} ionic radius decreases further, progressively larger and larger proportions of the SAP isomer are observed (Fig. 6).

The shift pattern of one of the two *S-SSSS*-Eu**2**$^{3+}$ regioisomeric chelates appears to exactly mirror that of the only regioisomeric chelate isolated in our previously reported work on *S-SSSS*-Eu**1**$^{-}$ [22]. This *S-SSSS*-Eu**1**$^{-}$ chelate also existed as a mixture of SAP and TSAP isomers; interestingly, we found the proportions of each to be the same in each of these chelates: 5 % SAP and 95 % TSAP. Furthermore, the distribution of the coordination geometries in either *S-SSSS*-Eu**2**$^{3+}$ or *S-SSSS*-Yb**2**$^{3+}$ was found to be insensitive to either changes in temperature or solvent (Fig. S2), in marked contrast to the behavior of some other related chelates [32]. Apparently, differences in the nature of the amide substituent—smaller and hydrophilic for *S-SSSS*-Eu**1**$^{-}$ and larger and hydrophobic for *S-SSSS*-Eu**2**$^{3+}$—have little or no effect on the preferred coordination geometry distribution of the chelate.

The identity of each chelate of *S-SSSS*-Eu**2**$^{3+}$ obtained was also determined through examination of the ax^{S} couplings in an ^{1}H–^{1}H COSY spectrum (Fig. 7). Using the same logic applied in the analysis of the COSY spectrum of *S-RRRR*-Eu**2**$^{3+}$ (Fig. 4) and the Karplus relationship, one can identify the two TSAP ax^{S} protons located on the same ethylene bridge as the nitrobenzyl group. The most shifted ax^{S} resonance (a little downfield of 15 ppm) is found to have three couplings, two vicinal couplings and a nuclear Overhauser effect cross-peak correlated with a benzylic

proton. The absence of a geminal coupling and the presence of the nuclear Overhauser effect cross-peak correlated with a benzylic proton is clear evidence that this proton is located on the same carbon as the nitrobenzyl substituent; i.e., this is a "side isomer". One more observation of note is that the ax^S–eq^C vicinal coupling is weaker in this case than the same couplings in other ethylene bridges of the same chelate. This is in direct contrast to the observation made for the side isomer of *S-RRRR*-Eu**2**$^{3+}$, for which the equivalent coupling was found to be stronger, but consistent with the observation made for NB-DOTMA chelates [27]. On the basis of the Karplus relationship, this suggests that the nitrobenzyl substituent distorts the gauche conformation of the ethylene bridge on which it is located in such a way as to increase the ax^S–eq^C angle (Φ). One other resonance is found to have only two *J* couplings, one that is shifted to about 12.5 ppm. In this case, however, the couplings are clearly one geminal ax^S–eq^S coupling and one vicinal ax^S–ax^C coupling. In other words this proton is also located on the same ethylene bridge as the nitrobenzyl group, but in this case the substituent is located on the corner carbon. Thus, we may conclude that here again we observe a mixture of "side" and "corner" isomers. It is worth reiterating our note of caution against the temptation to examine the distribution of side and corner isomers across the series, because here again the experiments were not conducted in such a manner as to allow such an analysis. On the basis of the shift pattern, the single SAP isomer observed in the spectrum of *S-SSSS*-Eu**2**$^{3+}$ appears to be a side isomer. Owing to the low concentrations of this structure only geminal *J* couplings are observed in the COSY spectrum, and although one must be circumspect in examining the absence of cross-peaks, the absence of a geminal coupling to the most shifted SAP resonance is consistent with the assignment of this as a side isomer.

The assignment of this SAP isomer as a side isomer is confirmed by analysis of the ax^S chemical shifts of *S-SSSS*-Eu**2**$^{3+}$ as a function of temperature (Fig. 8). Here again we observe that although the absolute shifts of each TSAP resonance decrease with increasing temperature, there is no movement of the side and corner isomers towards one another. This confirms that the side and corner isomers are not in chemical exchange with one another. Interestingly, the chemical shifts of four ax^S protons from one of the TSAP isomers decrease at a slower rate with increasing temperature than those of the other four. This appears to be the result of chemical exchange between this TSAP isomer and the single SAP isomer that is observed. This affords an unambiguous assignment of these four TSAP ax^S protons to the same structure, the side isomer. Examining the shift patterns of the two coordination geometries of the side isomer of *S-SSSS*-Eu**2**$^{3+}$ and those of the reported isomer

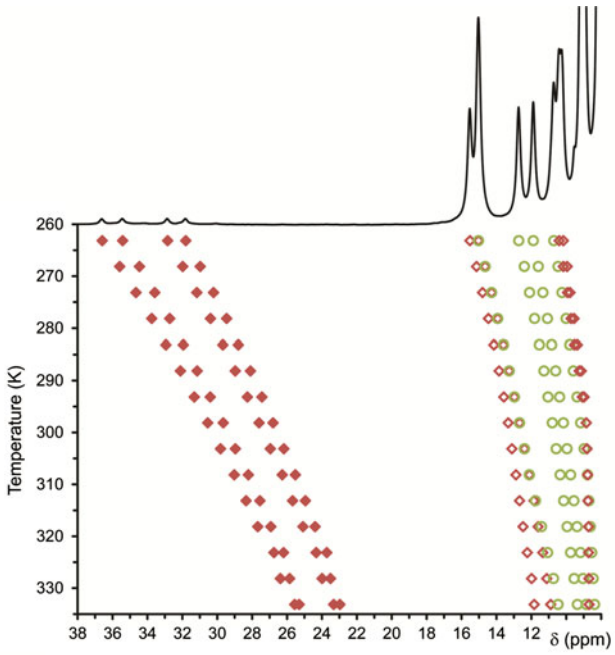

Fig. 8 The effect of temperature on the shifts of the ax^S proton resonances of *S-SSSS*-Eu**2**$^{3+}$ in CD_3OD at 400 MHz. The corner isomer is denoted by the *circles* and is found to adopt solely a TSAP coordination geometry. The side isomer is denoted by *diamonds* and is observed in both the SAP coordination geometry (*filled symbols*) and the TSAP coordination geometry (*open symbols*)

of *S-SSSS*-Eu**1**$^-$, in conjunction with population distribution data, reveals that the isomer of *S-SSSS*-Eu**1**$^-$ reported previously must also have been a side isomer.

These variable-temperature data conclusively demonstrate that the SAP and TSAP coordination geometries of the side isomer of *S-SSSS*-Eu**2**$^{3+}$ are in chemical exchange that is slow on the NMR timescale. It is noteworthy that evidence for this same exchange in the side isomer of *S-SSSS*-Eu**1**$^-$ was not found, which does not mean that exchange is not occurring in this case, just that it was not observed. In fact, in light of the observed evidence for exchange in the side isomer of *S-SSSS*-Eu**2**$^{3+}$, it seems more likely than not that a SAP ↔ TSAP chemical equilibrium exists for the side isomer of *S-SSSS*-Eu**1**$^-$.

As the ionic radius of the Ln^{3+} ion decreases yet further from Eu^{3+} to Yb^{3+}, progressively more and more SAP geometry is observed for each chelate (Figs. 6, 9). Notably a SAP geometry of the corner isomer, absent for Eu^{3+}, is eventually observed for the later lanthanides. The SAP/TSAP distribution is never the same between the side and corner isomers for any given Ln^{3+} ion. Figure 9 shows the distribution of SAP and TSAP isomers for the corner and side isomers of some *S-SSSS*-Ln**2**$^{3+}$ chelates across the series. In many cases the paramagnetic line broadening of the Ln^{3+} ion precludes an accurate determination of these ratios, leaving only six data points across the series to

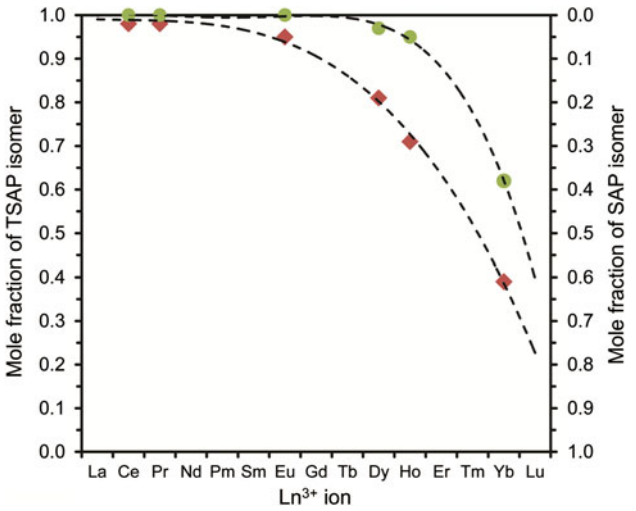

Fig. 9 The distribution of SAP [Λ(δδδδ)] and TSAP [Δ(δδδδ)] coordination geometries of the side (*diamonds*) and corner (*circles*) isomers of *S-SSSS*-Ln**2**$^{3+}$. The *dashed lines* are a guide for the eye

illustrate the trend. The assignment of "side" or "corner" was made on the basis of the shift pattern of the ax^S protons, which appears to be quite consistent over all Ln^{3+} ions and SAP and TSAP isomers. The side isomer is generally characterized by the four resonances appearing in two pairs, whereas the corner isomer is characterized by resonances appearing in one pair, with the other resonances shifted further away, one upfield and one downfield (Figs. 3, 5, 6, 8).

Despite the relatively low number of data points, the trend in the isomeric ratios is quite clear. As with other related systems, the TSAP geometry is favored by the larger, early Ln^{3+} ions, whereas the SAP geometry is increasingly favored by the smaller, later Ln^{3+} ions. It is noteworthy that this preference is considerably more pronounced and occurs earlier in the series for the side isomer of *S-SSSS*-Ln**2**$^{3+}$. However, the situation for chelates of *S-SSSS*-Ln**2**$^{3+}$ is not directly comparable to that in previously published studies of DOTA and DOTA-tetraamide chelates [43, 47–49]. As discussed earlier, the presence of the chiral amide substituents renders rotation of the pendant arms from Δ to Λ an energetically unfavorable process. Conversion of the Δ(δδδδ) TSAP isomer to the Λ(δδδδ) SAP isomer can occur only through this arm rotation process. Thus, a TSAP to SAP conversion will occur only if this energy penalty is offset by the chelate adopting a SAP geometry. Clearly this offset is greater for the side isomer, which more readily adopts a SAP geometry, even with moderately sized Ln^{3+} ions. This suggests that the coordination "cage" afforded by the side isomer is more suited to the accommodation of smaller Ln^{3+} ions; i.e., it is significantly smaller than that afforded by the corner isomer. A clue to how the coordination cage differs may be found in the aforementioned shift patterns of the ax^S protons. The LIS of these protons is almost exclusively the result of a through-space dipolar shift, which is dependent on the spatial location of the proton relative to the metal ion and the magnetic field induced by the metal ion within its ligand field. It is now evident that chelates based on NB-cyclen are substantially distorted relative to their cyclen-based counterparts. However, the uniform differences in the ax^S shift pattern indicate that the two regioisomeric chelates distort differently. This distortion may result in a difference in the spatial positioning of the protons in the ligand, which, if reflected in the arrangement of the ligating donor atoms, could lead to a significant nonaxial component of the magnetic susceptibility tensor. It seems most likely both of these occur in these chelates. The resulting ax^S shift patterns appears to have a good deal in common with the ax^S shift pattern observed for a bridged DOTA-tetraamide chelate [48]. The side isomers of Ln**2**$^{3+}$ more closely resemble the diagonally distorted bridged Yb^{3+} chelates, and the corner isomers resemble the asymmetrically distorted Pr^{3+} chelates [48]. Such a difference in the way in which the regioisomeric chelates distort could give rise to the difference in the size of the coordination cage and their isomeric distributions. If so, it could also be expected to have a profound effect on the behavior of the coordinated water molecule and therefore the CEST properties of the chelates.

Water exchange and saturation transfer experiments

It is now well established that the kinetics of water proton exchange are substantially reduced in aprotic solvents such as acetonitrile [33]. Studying the chelates in acetonitrile solution aids direct observation and assessment of water molecules coordinated to the Ln^{3+} center. To observe the coordinated water molecules under conditions of minimal line-broadening, ^{1}H NMR spectra of *S-RRRR*-Pr**2**$^{3+}$, *S-RRRR*-Nd**2**$^{3+}$, *S-RRRR*-Eu**2**$^{3+}$, *S-SSSS*-Pr**2**$^{3+}$, S-*SSSS*-Eu**2**$^{3+}$ were recorded at 275 K in CD_3CN with a minimum of H_2O added (Figs. 10, S3). The resulting spectra contain two resonances corresponding to coordinated water molecules, clearly resolving the resonances from each of the two regioisomeric chelates present in each sample. In the spectrum of *S-SSSS*-Pr**2**$^{3+}$ (Fig. 10, top) the resonances of water coordinated to the side and corner isomers of the TSAP geometry are only barely resolved; the shift difference is very small. Furthermore, the intensity of each resonance is approximately equivalent, consistent with roughly equal amounts of each regioisomer, rendering it impossible to accurately identify which peak corresponds to which diastereoisomer or whether there is a difference in the exchange rate between the two. In contrast, the two resonances of water coordinated to the two regioisomers of

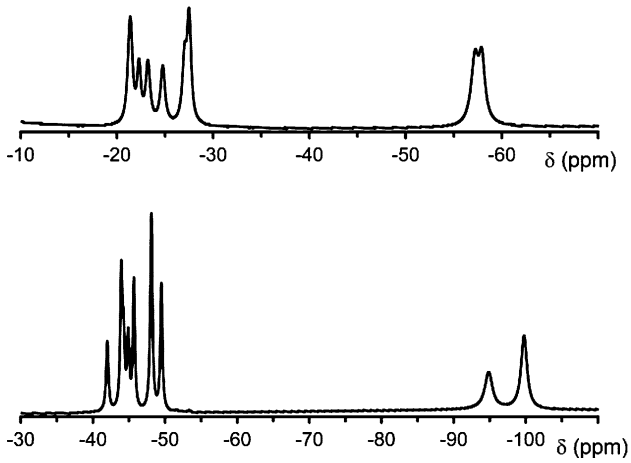

Fig. 10 The ^{1}H NMR spectra of *S-SSSS*-Pr**2**$^{3+}$ (*top*) and *S-RRRR*-Pr**2**$^{3+}$ (*bottom*) in 0.2 % *w/v* H_2O in CD_3CN at 263 K at 400 MHz, clearly showing the resonances of the water molecules associated with metal coordination in each regioisomeric chelate

the SAP isomer in the spectrum of *S-RRRR*-Pr**2**$^{3+}$ are very well resolved, with a shift difference somewhat more than 5 ppm. Furthermore, because the two regioisomers are present in unequal proportions, it is possible to assign each resonance to its regioisomer: the more shifted water resonance is that coordinated to the side isomer. It is notable that the resonance from the side isomer is somewhat narrower than that from the corner isomer, and this may be an indication that exchange of these water protons with those of the water in the solvent is slower than for those of the corner isomer. However, one must also take into account that the H_2O^{bound}/H_2O^{free} ratio is different for the two regioisomers of this chelate in this sample (the H_2O^{free} concentration is comparatively small) and this complicates a direct analysis of these data. By way of comparison, the ^{1}H NMR spectra of *S-RRRR*-Nd**2**$^{3+}$ and *S-RRRR*-Eu**2**$^{3+}$ (Fig. S3) also show two resolved coordinated water resonances. However, in each of these cases the amounts of each regioisomer present are more equal and the coordinated water resonances of each regioisomer are quite similar in shape. Notably in the spectrum of *S-SSSS*-Eu**2**$^{3+}$ no resonances corresponding to a coordinated water molecule are observed, suggesting that for both regioisomeric TSAP chelates the water proton exchange rate increases rapidly as the Ln^{3+} ionic radius decreases.

Assessment of water exchange kinetics is more readily achieved in these types of DOTA-tetraamide chelate by means of CEST experiments. The effectiveness of a chelate as a CEST agent is assessed by recording its "CEST spectrum". This is achieved by measuring the intensity of the solvent water peak as a function of the frequency offset of a soft presaturation pulse. CEST spectra were recorded under similar conditions—minimal water in CD_3CN and 263 K—for the same five chelates. When the presaturation

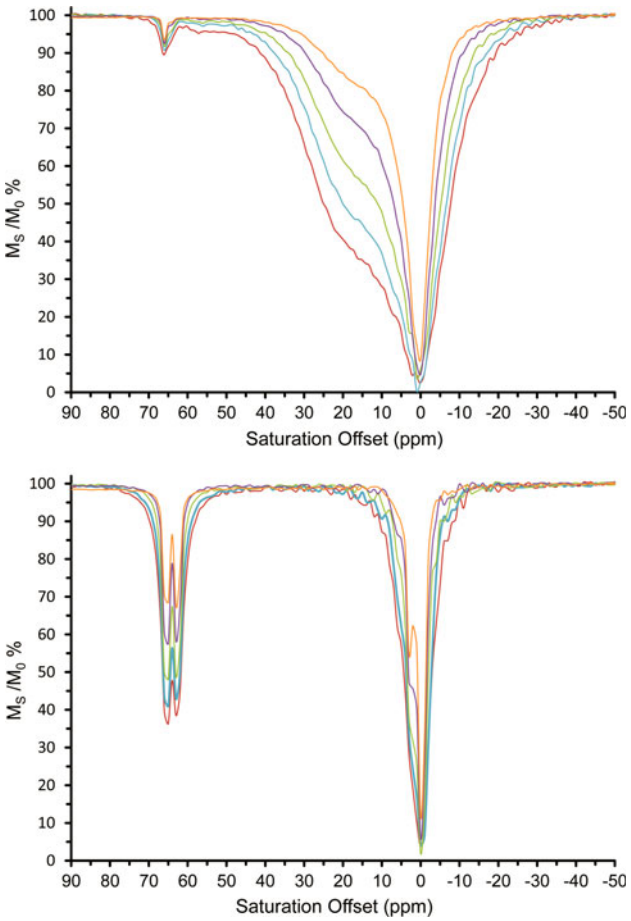

Fig. 11 The chemical exchange saturation transfer (CEST) spectra of 6.775 mM (Eu^{3+}) solutions of *S-SSSS*-Eu**2**$^{3+}$ (*top*) and *S-RRRR*-Eu**2**$^{3+}$ (*bottom*) recorded at 263 K and 400 MHz in CD_3CN with 1.1 % w/v H_2O, using a $\boldsymbol{B}_1$ presaturation pulse of 10 s at 148 Hz (*orange lines*), 203 Hz (*purple lines*), 279 Hz (*green lines*), 350 Hz (*cyan lines*), and 446 Hz (*red lines*)

pulse applied was of sufficiently low power, it was possible to resolve separate CEST peaks for the side and corner regioisomers of both *S-RRRR*-Pr**2**$^{3+}$ and *S-SSSS*-Pr**2**$^{3+}$ (Fig. S4). Similarly, in the CEST spectra of *S-RRRR*-Nd**2**$^{3+}$ (Fig. S4) and *S-RRRR*-Eu**2**$^{3+}$ (Fig. 11) one CEST peak is resolved for water coordinated to each regioisomer in solution. Given the wealth of information on the CEST of Eu^{3+} chelates, for this study we chose to focus our attention on the two stereoisomeric Eu**2**$^{3+}$ chelates. The CEST spectra of *S-RRRR*-Eu**2**$^{3+}$ are rather unusual; CEST from two coordinated water molecules is observed. Also observed at various stages over the selected $\boldsymbol{B}_1$ power range, are CEST peaks arising from several amide protons close to the peak arising from direct saturation of water at 0 ppm. These peaks are of note because in general the CEST peaks from amide protons in SAP isomers of the EuDOTA-tetraamide chelate are observed slightly upfield of the direct saturation peak. However, in the spectrum of

S-RRRR-Eu**2**$^{3+}$ CEST peaks of differing intensities can be observed both upfield and downfield of the direct saturation peak. This leads us to conclude that the distortion of the DOTA framework induced by the nitrobenzyl group, discussed earlier, has two effects on the amide protons. Firstly, it alters the electronic distribution in each arm, causing the amide protons of each pendant arm to exchange at different rates, hence the differences in intensity on changing the $\boldsymbol{B}_1$ power. Secondly, it causes unusual LIS of each of these protons, shifting some upfield and others downfield.

In principle CEST is limited by the slow exchange condition ($k_{ex} \leq \Delta\omega$), but in practice it is often possible to observe CEST from resonances that exchange slightly faster than this limit. For example, in the CEST spectrum of *S-SSSS*-Eu**2**$^{3+}$, a broad CEST peak is observed arising from the rapidly exchanging water protons of the TSAP isomers even though peaks from these resonances are not visible in the ^{1}H NMR spectrum (Fig. S3). This CEST peak is centered at about +25 ppm, consistent with water coordinated to Eu^{3+} in a TSAP coordination geometry but much too far from the direct saturation peak to arise from an amide proton of the pendant arm. However, the spectrum is most notable for the small CEST peak arising from the side SAP isomer at 66 ppm. This peak arises from a species that is present in only very low quantities; constituting slightly less than 5 % of the side isomer, its overall concentration in solution is just 0.14 mM. Although it is present in only small quantities, this chelate is able to generate a comparatively large CEST effect. The CEST arising from this chelate on a per millimole basis is much larger than that arising from either regioisomer of *S-RRRR*-Eu**2**$^{3+}$. CEST is highly sensitive to a number of variables, so unlike Gd^{3+} chelates there is no single parameter that quantifies the effectiveness of an agent in the manner of relaxivity. However, because the data for each Eu**2**$^{3+}$ chelate were acquired under identical conditions, it is possible to make comparisons across these data (and only these data) by calculating the percent CEST generated by the chelate on a per millimolar basis for each $\boldsymbol{B}_1$ power used (Table 1). The "effectiveness" of the side SAP isomer of *S-SSSS*-Eu**2**$^{3+}$ as a CEST agent is between 3.6 and 4.5 times greater than that of either regioisomer of *S-RRRR*-Eu**2**$^{3+}$.

It is significant that the greatest difference in the effectiveness of the side SAP isomers of *S-SSSS*-**2**$^{3+}$ and *S-RRRR*-**2**$^{3+}$ is at the lowest $\boldsymbol{B}_1$ power. To meet specific absorption rate restrictions in MRI examinations it is imperative that the maximum amount of CEST be generated from the lowest possible $\boldsymbol{B}_1$ powers. From Woessner's analysis of the Bloch equations modified for exchange [14, 50], it is clear that to achieve this it is necessary to have very slow proton exchange kinetics. The fact that *S-SSSS*-Eu**2**$^{3+}$ has higher potency as a CEST agent at the lowest presaturation power ($\boldsymbol{B}_1$ power of 148 Hz), of all three SAP isomers is suggestive that our initial hypothesis is correct—forcing the phenyl substituents into a pseudoaxial position slows exchange. It is common practice to determine exchange kinetics by fitting the CEST spectrum to the Bloch equations modified for exchange. In the present cases, such an analysis is prohibited by the presence of a large (11 or 16) number of potentially unique exchanging pools in each spectrum. Given the large number of variables involved in each analysis (upwards of 33), a number that could not reasonably be reduced, this is clearly not a scientifically robust method for analyzing these data. Instead we chose to use the Dixon–Sherry "omega method," in which the CEST generated is plotted as a function of the presaturation $\boldsymbol{B}_1$ power to afford the proton residence lifetime as the intercept of the *x*-axis [51]. The omega plots for both regioisomers of *S-RRRR*-**2**$^{3+}$ afford straight lines as expected. Each isomer has a different CEST response to changing the $\boldsymbol{B}_1$ power; the omega plot reveals that this originates from a difference in the water proton exchange rate (Fig. 12, Table 1). This result is rather unexpected; it suggests that even relatively small distortions to the lanthanide coordination cage can have subtly different effects on water proton exchange. It is worthy of note that in these Eu^{3+} chelates it is the *more* shifted water that appears to exchange more quickly. In contrast, for the Pr^{3+} chelates, it appeared that the *less* shifted corner isomer underwent more rapid exchange (Fig. 10). No assignment of each water proton resonance to an individual regioisomer of *S-RRRR*-Eu**2**$^{3+}$ could be

Table 1 Parameters relevant to the chemical exchange saturation transfer (*CEST*) spectra shown in Fig. 11 for the three square antiprismatic (SAP) isomers of Eu**2**$^{3+}$ (for the structure, see Fig. 1)

	Peak (ppm)	Eu**2** (mM)	τ_M^H (ms)	CEST (%/mM)				
				148 Hz	203 Hz	279 Hz	350 Hz	446 Hz
S-RRRR-Eu**2**$^{3+}$	63	3.14	3.70	10.4	13.3	16.3	18.2	19.6
	65	3.64	3.15	8.6	11.7	14.3	16.2	17.5
S-SSSS-Eu**2**$^{3+}$	66	0.14	4.68–10.6	47.1	53.4	58.7	66.2	74.2

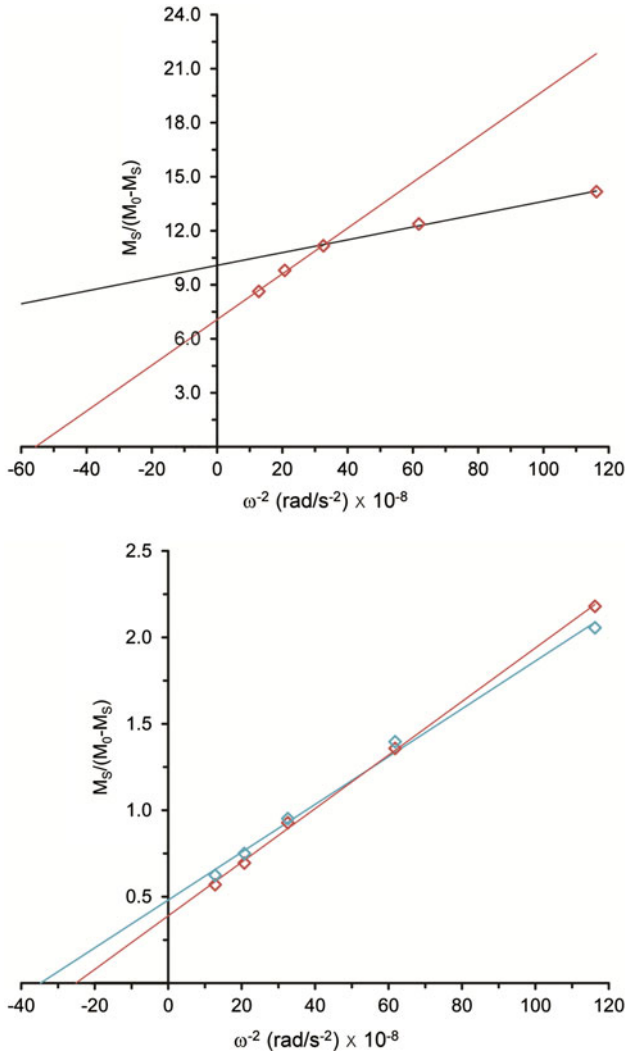

Fig. 12 Omega plots generated from the CEST data of the three SAP isomers of Eu**2**$^{3+}$ shown in Fig. 11; *top S-SSSS*-Eu**2**$^{3+}$ and *bottom S-RRRR*-Eu**2**$^{3+}$ (*blue line* 63 ppm, *red line* 65 ppm)

made; the effectively equal distribution of corner and side isomers in the sample means there is no basis for discriminating one from the other. As a consequence, it is not possible to conclude whether the same regioisomer exchanges most rapidly for both *S-RRRR*-Pr**2**$^{3+}$ and *S-RRRR*-Eu**2**$^{3+}$ or whether it is a different isomer for each Ln^{3+} ion. It is conceivable that the exchange rate differs between corner and side isomers with differing Ln^{3+} ions and the most rapidly exchanging regioisomer may not consistently be the same.

The omega plot for the SAP side isomer of *S-SSSS*-Eu**2**$^{3+}$ is nonlinear; there is a clear inflection point around the middle of the data. It is not clear why this should be. One can speculate that this could arise for a number of reasons: there is excessive noise or error in the data; the theory on which this plot is based breaks down when exchange is very, very slow; the involvement of CD_3CN in the exchange process, when exchange is slow, interferes with the model; or possibly the theory is undermined by the presence of other abundant exchanging pools. With only one anomalous data set it is not currently possible to determine the origin of this nonlinearity. The nonlinearity of the data means that they cannot be simply fitted using linear regression analysis to afford the exchange rate. However, by fitting these data to each extreme (Fig. 12), one can generate a range within which the exchange rate must fall (Table 1). This exercise shows that the water proton residence lifetime lies in the range 4.6–10.4 ms. Although this is quite a wide range, it is substantially longer than the water proton residence lifetimes for either regioisomer of *S-RRRR*-Eu**2**$^{3+}$, which are between 3.1 and 3.7 ms. Although these water proton residence lifetimes are all very long in comparison with those usually observed for the DOTA-tetraamide chelates in aqueous solution, it must be noted that these data were acquired at very low temperatures (just 263 K) and with very low water concentrations (611 mM compared with 55.6 M in H_2O).

Conclusions

The problems encountered in separating the side and corner regioisomers of Ln**2**$^{3+}$ chelates have provided many more insights into the coordination chemistry of nitrobenzyl-substituted chelates than were gained from our initial studies into Ln**1**$^{-}$ chelates alone. Significantly, the preference for coordination geometry follows the same overall trend that was observed for the Ln**1**$^{-}$ chelates: the *S-RRRR* isomer exhibits a preference for the SAP coordination geometry across the series and the *S-SSSS* isomer exhibits a preference for the TSAP isomer, but with increasing amounts of SAP isomer observed as the Ln^{3+} ionic radius decreases. The amount of SAP isomer present differs for the side and corner regioisomers, hinting at a difference in the size of the coordination cage between the two regioisomers. The idea that the central Ln^{3+} ion is differentially crowded by the two regioisomers is supported by the observation that the water proton exchange kinetics of the side and corner isomers are not the same. Finally, we find that placing large amide substituents into a pseudoaxial position (Fig. 2) can have substantial and unexpected effects on the water proton pool and its exchange characteristics. In the case of *S-SSSS*-Ln**1**$^{-}$, the pseudoaxial carboxylates of the SAP isomer appear to recruit additional protons into the "bound water" pool, enhancing CEST. In the case of *S-SSSS*-Ln**2**$^{3+}$, the pseudoaxial phenyl groups of the SAP isomer appears to substantially slow the water exchange kinetics of the chelate. This affords a chelate that is as much as 4.5 times more effective as a CEST agent than an isomeric chelate with the phenyl substituents in the

pseudoequatorial position. Clearly, the conditions under which these chelates have been studied do not approach those prevailing physiologically. Several modifications would need to be made to these systems before they could be useful as CEST agents for MRI. Ideally the agent would adopt exclusively the conformation of the SAP isomer observed for *S-SSSS*-Eu**2**$^{3+}$. The chelates would need to be rendered both nontoxic (as these tricationic chelates are almost not well tolerated in vivo) [52] and made water-soluble; both of these prerequisites could be achieved through incorporation of three or four anionic groups, such as carboxylates, into the chelate structure [52].

Acknowledgments The authors thank the National Institutes of Health (EB-11687), the Oregon Nanoscience and Microtechnologies Institute (N00014-11-1-0193), Portland State University, and the Oregon Opportunity for Biomedical Research for financial support of this work.

References

1. Zhang S, Winter P, Wu K, Sherry AD (2001) J Am Chem Soc 123:1517–1518
2. Sherry AD, Zhang S, Woods M (2005) In: Sessler JL, Doctrow SR, McMurray TJ, Lippard SJ, (eds) Medicinal inorganic chemistry. ACS symposium series 903. American Chemical Society, Washington, pp 151–165
3. Ward KM, Aletras AH, Balaban RS (2000) J Magn Reson 143:79–87
4. Bonnet CS, Toth E (2010) Am J Neuroradiol 31:401–409
5. Dorazio SJ, Morrow JR (2012) Eur J Inorg Chem 2012:2006–2014
6. Gianolio E, Stefania R, Di Gregorio E, Aime S (2012) Eur J Inorg Chem 2012:1934–1944
7. Hancu I, Dixon WT, Woods M, Vinogradov E, Sherry AD, Lenkinski RE (2010) Acta Radiol 51:910–923
8. Pacheco-Torres J, Calle D, Lizarbe B, Negri V, Ubide C, Fayos R, Larrubia Pilar L, Ballesteros P, Cerdan S (2011) Curr Top Med Chem 11:115–130
9. Sherry AD, Woods M (2007) In: Modo MMJ, Bulte JWM (eds) Molecular and cellular MR imaging. CRC, Boca Raton, pp 101–122
10. Terreno E, Delli Castelli D, Aime S (2010) Contrast Media Mol Imaging 5:78–98
11. Tsitovich PB, Morrow JR (2012) Inorg Chim Acta 393:3–11
12. Viswanathan S, Kovacs Z, Green KN, Ratnakar SJ, Sherry AD (2010) Chem Rev 110:2960–3018
13. Winter PM (2012) Wiley Interdiscip Rev Nanomed Nanobiotechnol 4:389–398
14. Woods M, Woessner DE, Sherry AD (2006) Chem Soc Rev 35:500–511
15. Ali MM, Bhuiyan MPI, Janic B, Varma NRS, Mikkelsen T, Ewing JR, Knight RA, Pagel MD, Arbab AS (2012) Nanomedicine 7:1827–1837
16. Ali MM, Yoo B, Pagel MD (2009) Mol Pharm 6:1409–1416
17. Ferrauto G, Delli Castelli D, Terreno E, Aime S (2013) Magn Reson Med 69:1703–1711
18. Li AX, Suchy M, Li C, Gati JS, Meakin S, Hudson RHE, Menon RS, Bartha R (2011) Magn Reson Med 66:67–72
19. Liu G, Li Y, Shethy VR, Pagel MD (2012) Mol Imaging 11:47–57
20. Sheth VR, Li Y, Chen LQ, Howison CM, Flask CA, Pagel MD (2012) Magn Reson Med 67:760–768
21. Yoo B, Sheth VR, Howison CM, Douglas MJK, Pineda CT, Maine EA, Baker AF, Pagel MD (2013) Magn Reson Med. doi:10.1002/mrm.24763.
22. Carney CE, Tran AD, Wang J, Schabel MC, Sherry AD, Woods M (2011) Chem Eur J 17:10372–10378
23. Woods M, Kovacs Z, Zhang S, Sherry AD (2003) Angew Chem Int Ed 42:5889–5892
24. Woods M, Botta M, Avedano S, Wang J, Sherry AD (2005) Dalton Trans 3829–3837
25. Di Bari L, Pescitelli G, Sherry AD, Woods M (2005) Inorg Chem 44:8391–8398
26. Tircso G, Webber BC, Kucera BE, Young VG, Woods M (2011) Inorg Chem 50:7966–7979
27. Webber BC, Woods M (2012) Inorg Chem 51:8576–8582
28. Graham B, Loh CT, Swarbrick JD, Ung P, Shin J, Yagi H, Jia X, Chhabra S, Barlow N, Pintacuda G, Huber T, Otting G (2011) Bioconjug Chem 22:2118–2125
29. Ranganathan RS, Raju N, Fan H, Zhang X, Tweedle MF, Desreux JF, Jacques V (2002) Inorg Chem 41:6856–6866
30. Baranyai Z, Banyai I, Brucher E, Kiraly R, Terreno E (2007) Eur J Inorg Chem 2007:3639–3645
31. Thompson AL, Parker D, Fulton DA, Howard JAK, Pandya SU, Puschmann H, Senanayake K, Stenson PA, Badari A, Botta M, Avedano S, Aime S (2006) Dalton Trans 5605–5616
32. Miller KJ, Saherwala AA, Webber BC, Wu Y, Sherry AD, Woods M (2010) Inorg Chem 49:8662–8664
33. Woods M, Pasha A, Zhao P, Tircso G, Chowdhury S, Kiefer G, Woessner DE, Sherry AD (2011) Dalton Trans 40:6759–6764
34. Dickins RS, Parker D, Bruce JI, Tozer DJ (2003) Dalton Trans 1264–1271
35. Thompson AL, Parker D, Fulton DA, Howard JAK, Pandya SU, Puschmann H, Senanayake K, Stenson PA, Badari A, Botta M, Avedano S, Aime S (2006) Dalton Trans 5605–5616
36. Frias JC, Bobba G, Cann MJ, Hutchison CJ, Parker D (2003) Org Biomol Chem 1:905–907
37. Parker D, Dickins RS, Puschmann H, Crossland C, Howard JAK (2002) Chem Rev 102:1977–2010
38. Aime S, Barge A, Batsanov AS, Botta M, Castelli DD, Fedeli F, Mortillaro A, Parker D, Puschmann H (2002) Chem Commun 1120–1121
39. Woods M, Zhang S, Von Howard E, Sherry AD (2003) Chem Eur J 9:4634–4640
40. Meyer M, Dahaoui-Gindrey V, Lecomte C, Guilard L (1998) Coord Chem Rev 180:1313–1405
41. Aime S, Botta M, Ermondi G, Terreno E, Anelli PL, Fedeli F, Uggeri F (1996) Inorg Chem 35:2726–2736
42. Adair C, Woods M, Zhao PY, Pasha A, Winters PM, Lanza GM, Athey P, Sherry AD, Kiefer GE (2007) Contrast Media Mol Imaging 2:55–58
43. Woods M, Kovacs Z, Kiraly R, Brücher E, Zhang S, Sherry AD (2004) Inorg Chem 43:2845–2851
44. Marques MPM, Geraldes CFGC, Sherry AD, Merbach AE, Powell H, Pubanz D, Aime S, Botta M (1995) J Alloys Compd 225:303–307
45. Karplus M (1963) J Am Chem Soc 85:2870–2871
46. Aime S, Botta M, Ermondi G (1992) Inorg Chem 31:4291–4299
47. Aime S, Botta M, Fasano M, Marques MPM, Geraldes CFGC, Pubanz D, Merbach AE (1997) Inorg Chem 36:2059–2068
48. Vipond J, Woods M, Zhao P, Tircso G, Ren JM, Bott SG, Ogrin D, Kiefer GE, Kovacs Z, Sherry AD (2007) Inorg Chem 46:2584–2595

49. Aime S, Botta M, Garda Z, Kucera BE, Tircso G, Young VG, Woods M (2011) Inorg Chem 50:7955–7965
50. Woessner DE, Zhang S, Merritt ME, Sherry AD (2005) Magn Reson Med 53:790–799
51. Dixon WT, Ren J, Lubag AJM, Ratnakar J, Vinogradov E, Hancu I, Lenkinski RE, Sherry AD (2010) Magn Reson Med 63:625–632
52. Woods M, Caravan P, Geraldes CFGC, Greenfield MT, Kiefer GE, Lin M, McMillan K, Prata MIM, Santos AC, Sun X, Wang J, Zhang S, Zhao P, Sherry AD (2008) Invest Radiol 43:861–870